Available online at www.sciencedirect.com

ScienceDirect

www.elsevier.com/locate/jes

JES JOURNAL OF ENVIRONMENTAL SCIENCES

www.jesc.ac.cn

Band gap tuning of g-C_3N_4 via decoration with AgCl to expedite the photocatalytic degradation and mineralization of oxalic acid

Hanlu Shi[1], *Rui He*[1], *Lei Sun*[1], *Gang Cao*[1], *Xiangjuan Yuan*[1,2,*], *Dongsheng Xia*[1,2,*]

1. *School of Environmental Engineering, Wuhan Textile University, Wuhan 430073, China*
2. *Engineering Research Center for Clean Production of Textile Dyeing and Printing, Ministry of Education, Wuhan 430073, China*

ARTICLE INFO

Article history:
Received 3 January 2019
Revised 10 April 2019
Accepted 11 April 2019
Available online 19 April 2019

Keywords:
AgCl
Graphitic carbon nitride
Photocatalytic degradation
Oxalic acid
Mechanism

ABSTRACT

A series of functional organic–metal AgCl-decorated graphitic carbon nitride (AgCl-CN_x) composites were synthesized and applied for the degradation of oxalic acid (OA) under visible light. The highest photocatalytic activity was achieved with AgCl decoration ratio of 1.0 (denoted as AgCl-$CN_{1.0}$). The pseudo-first-order constant for OA degradation was 0.0722 min^{-1} with the mineralization efficiency of 90.80% after 60 min reaction in the photocatalytic process with AgCl-$CN_{1.0}$. A variety of characterization techniques including Brunauer–Emmett–Teller, X-ray diffraction, scanning electron microscope, transmission electron microscopy, X-ray photoelectron spectroscopy, Fourier transform infrared spectra, ultraviolet–visible diffuse reflectance spectra, photoluminescence, and Mott–Schottky were utilized to elucidate the physicochemical, microstructure, and optical properties contributing to the improvement of the photocatalytic performance. The results showed that AgCl-$CN_{1.0}$ had an oblate flaky erythrocyte-like structure with a moderate band gap energy of ~3.00 eV. In addition, the effects of the key parameters (i.e., AgCl-$CN_{1.0}$ dosage, initial OA concentration, solution pH, and presence of natural organic matter) on OA degradation were systematically investigated. Radical scavenger experiments indicated that photogenerated holes, electrons, superoxide anion radicals, and hydroxyl radicals were the dominant reactive species. Moreover, AgCl-$CN_{1.0}$ exhibited excellent stability and reusability for OA degradation without detectable Ag^+ release in the solution over multiple reaction cycles. The efficient OA mineralization could be mainly ascribed to the moderate specific surface area, increased numbers of active sites, and effective interfacial charge transfer of AgCl-$CN_{1.0}$. Overall, the AgCl-$CN_{1.0}$ composite was demonstrated to be a highly efficient, stable, and recoverable photocatalyst.

Introduction

Photocatalysis using semiconducting catalysts is a sustainable technology enabling one to use light to drive catalytic reactions, such as energy conversion, hydrogen production, carbon dioxide reduction, contaminated water purification, etc. (Asadzadeh-Khaneghah et al., 2018; Asahi et al., 2001; Liu et al., 2018b). In particular, graphitic carbon

* *Corresponding authors. E-mails:* dongsheng_xia@wtu.edu.cn (Dongsheng Xia), yuanxiangjuan1986@outlook.com (Xiangjuan Yuan).

https://doi.org/10.1016/j.jes.2019.04.009
1001-0742 © 2019 The Research Center for Eco-Environmental Sciences, Chinese Academy of Sciences. Published by Elsevier B.V.

nitride (g-C_3N_4), a 2-dimensionalπ-conjugated polymeric metal-free semiconductor with a band gap energy (E_g) of ~2.7 eV, has attracted intensive attention worldwide, due to its unique physicochemical properties and electronic band structure (Mamba and Mishra, 2016; Patnaik et al., 2018). However, the photocatalytic efficiency of g-C_3N_4 needs further enhancement prior to any practical application, because of its high recombination rate of photogenerated charge carriers, narrow visible light absorption range and low specific surface area (<10 m^2/g) (Jiang et al., 2017; Mamba and Mishra, 2016; Patnaik et al., 2018; Zheng et al., 2012).

To date, several strategies including nano/mesoporous structure fabrication, semiconductor heterojunction construction, non-metal doping, and noble metal modification, have been applied to overcome the aforementioned disadvantages of g-C_3N_4 (Bellardita et al., 2018; Dong et al., 2018; Oh et al., 2018; Yuan et al., 2018a). Amongst these, the fabrication of heterostructured composites by combining g-C_3N_4 with different semiconductors of proper energy potential differences (e.g., $BiFeO_3$/g-C_3N_4, ZnO/g-C_3N_4, TiO_2/g-C_3N_4, $BiVO_4$/g-C_3N_4 Ag_3PO_4/g-C_3N_4, Al_2O_3/Cu/g-C_3N_4, BiOCl/Cu_2O/Fe_3O_4/g-C_3N_4, Ag_2O/g-C_3N_4, and FeOOH/g-C_3N_4) (An et al., 2016; Kumar et al., 2018; Li et al., 2018; Liang et al., 2019; Miao et al., 2018; Wang et al., 2018; Xu et al., 2018a; Yuan et al., 2018a; Qian et al., 2018), can not only efficiently restrict the recombination of photogenerated charge carriers, but also endow the composites with novel characteristics or/and enhanced photocatalytic properties by means of synergistic effects.

Furthermore, AgCl, as a wide band gap semiconductor with an indirect E_g of ~3.25 eV, has displayed some appealing properties (Liu et al., 2018d). In recent years, AgCl has been generally employed as a photosensitive material in the photographic film industry and has also been recognized as potential visible-light-driven photocatalyst for chemical pollutant degradation (Liao et al., 2013). For instance, a number of studies have indicated that the deposition of Ag or/and AgX (X = Cl, Br, I, etc.) on semiconductors could lead to excellent photocatalytic activity due to the induction of the surface plasmon resonance effect, further enhancing the visible light absorption and electron–hole ($e–h^+$) separation efficiencies of the photocatalyst (Asadzadeh-Khaneghah et al., 2018; Li et al., 2017; Liao et al., 2013). To the best of our knowledge, oxalic acid (OA) degradation via AgCl/g-C_3N_4 under visible light has been rarely reported. Based on the combination of AgCl and g-C_3N_4, the band gap can be tuned to effectively harvest visible light and the lifetime of photogenerated $e–h^+$ pairs can be extended due to the heterojunction structure.

Herein, a series of functional organic–metal AgCl-decorated g-C_3N_4 (AgCl-CN_x) composites were synthesized by a simple precipitation-reflux method. Meanwhile, the physiochemical, microstructure, and optical properties were well characterized by using various analytical techniques. OA, a common stable and final oxidation product of organic pollutants, was chosen as the probe compound to evaluate the photocatalytic activity. A systematic study was performed to investigate the effects of key parameters (i.e., photocatalyst dosage, initial OA concentration, solution pH, and natural organic matter (NOM)) on OA degradation under visible light. In addition, photoelectrochemical measurements were further applied to determine the band structure and evaluate the charge transfer capability of AgCl-CN_x composites. Moreover, a possible mechanism responsible for efficient OA degradation and mineralization was proposed.

1. Materials and methods

1.1. Chemicals and reagents

All the chemicals used in the experiments were analytical reagent grade and used directly without any further purification.

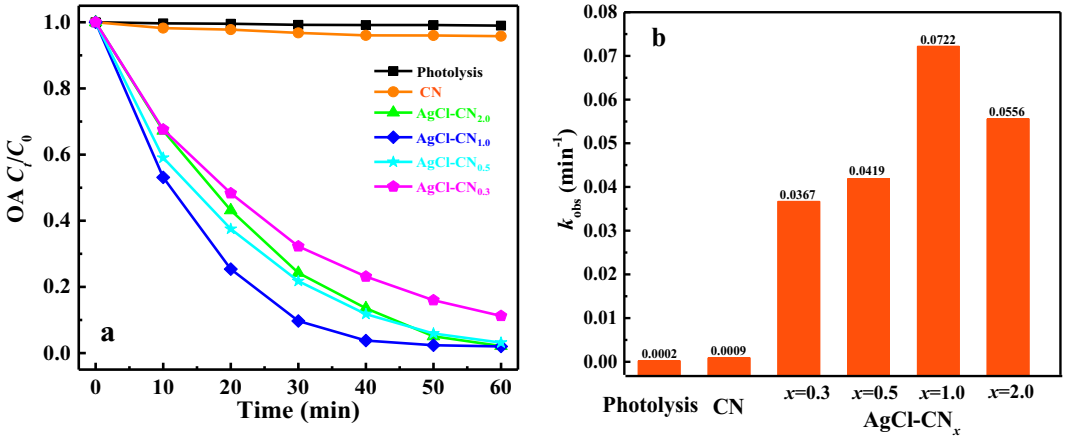

Fig. 1 – (a) Oxalic acid (OA) degradation efficiency and (b) pseudo-first-order constant (k_{obs}) of OA in different photocatalytic processes. Experimental conditions: initial concentration of OA ($[OA]_0$) = 50 mg/L, [CN] = [AgCl-CN_x] = 100 mg/L, initial pH (pH_0) = 6.0 ± 0.1, and temperature (T) = 20°C. C_t/C_0: the concentration of pollution at reaction time of t and 0; CN: graphitic carbon nitride; AgCl-CN_x: AgCl-decorated CN composites with different decoration ratios (x) of AgCl to CN; [CN]: concentration of CN; [AgCl-CN_x]: concentration of AgCl-CN_x.

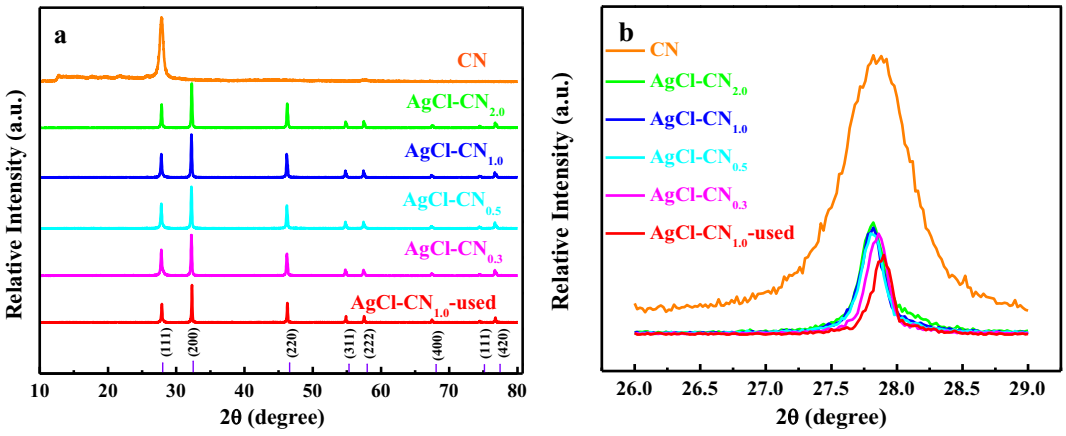

Fig. 2 – (a) X-ray diffraction patterns and (b) diffraction peaks centered at 27.8° of CN and AgCl-CN_x composites.

Silver sulfate (Ag_2SO_4), potassium chloride (KCl), OA, melamine, ethanol, barium sulfate ($BaSO_4$), *p*-benzoquinone (BQ), isopropanol (IPA), disodium ethylenediaminetetraacetate (Na_2-EDTA), potassium dichromate ($K_2Cr_2O_7$), etc. were supplied by Sinopharm Chemical Reagent, China. 5,5-Dimethyl-1-pyrolin-N-oxide (DMPO, purity > 97%) was purchased from Aladdin Industrial Corporation, China. Humic acid sodium salt (HA) was obtained from Sigma–Aldrich, USA. Ultrapure water (>18.2 MΩ·cm) obtained from a Millipore Milli-Q system (A10, Millipore, USA) was used for all the synthesis and treatment.

1.2. Preparation of photocatalysts

1.2.1. Preparation of g-C_3N_4

Bulk g-C_3N_4 was prepared by direct thermal condensation. Firstly, a certain amount of melamine was placed in an alumina crucible and heated at 550°C for 4 hr at a heating rate of 3°C/min in a muffle furnace. Then, the resultant yellow powder was subjected to a second calcination in a muffle furnace at 650°C for another 4 hr. After cooling down to room temperature, g-C_3N_4 was finally formed (denoted as CN).

1.2.2. Preparation of AgCl-CN_x composites

AgCl-CN_x composites were prepared via a simple precipitation-reflux method. Briefly, 0.3 g CN was dispersed in 150 mL ultrapure water and sonicated for 1 hr. Then, different amounts of Ag_2SO_4 (dissolved in 10 mL ultrapure water) were introduced into the solution under constant magnetic stirring for 2 hr. Subsequently, 20 mL KCl solution (0.117 mol/L) was added dropwise into the mixture. The obtained suspension was refluxed in a glycerol oil bath at 96°C for another 3 hr. Afterwards, the precipitate was washed three times with ultrapure water and dried at 60°C for 24 hr. The final production was denoted as AgCl-CN_x, in which *x* represented the decoration ratio of AgCl to CN (*x* = 0.3, 0.5, 1.0, and 2.0).

Table 1 – Specific surface areas, pore volumes, and mean pore diameters of CN and AgCl-CN_x composites.

Catalysts	Surface area (m^2/g)	Pore volume (cm^3/g)	Pore diameter (Å)
CN	44.7475	0.0701	62.6970
AgCl-$CN_{0.3}$	32.9834	0.0590	71.5522
AgCl-$CN_{0.5}$	23.9908	0.0441	73.4697
AgCl-$CN_{1.0}$	23.0696	0.0407	70.6267
AgCl-$CN_{2.0}$	6.1541	0.0109	70.8465

1.3. Characterization of photocatalysts

The physicochemical properties were recorded on an X-ray diffraction (XRD, X'Pert Pro MPD, PANalytical, Netherlands), Brunauer–Emmett–Teller (BET, ASAP 2010, Micromeritics, USA), Fourier transform infrared spectra (FT-IR, Nicolet iS5, Thermo Scientific, USA) and X-ray photoelectron spectroscopy (XPS, ESCALAB 250Xi, Thermo Scientific, USA). Morphological studies were carried out using a field emission scanning electron microscope (SEM, FEG 250, Quanta, USA) and the transmission electron microscopy (TEM, JEM-2100F, JEOL, Japan). Optical properties were measured on ultraviolet–visible diffuse reflectance spectra (UV–Vis DRS, U-4100, Hitachi, Japan) using $BaSO_4$ as the reference sample and photoluminescence spectra (PL, FP-6300, Jasco, Japan).

The photoelectrochemical measurements were carried out using an electrochemical workstation (CHI660E, CorrTest Instruments Corp, China) using a standard three-electrode quartz cell. The photoelectrodes were prepared by a dip-coating method. Photocatalyst (5 mg) was well-suspended in 1 mL ethanol and the slurry was then coated on the fluorine-doped tin oxide substrate (1 cm × 1 cm). The photoelectrode acted as the working electrode, the platinum wire and Ag/AgCl were used as the counter electrode and reference electrode, respectively. The electrolyte was 0.1 mol/L Na_2SO_4 solution. A 300 W Xenon lamp (PLS-SXE300, Perfectlight, China) was applied as a visible light source.

1.4. Evaluation of photocatalytic activity

OA was chosen as the target organic compound in this study to probe the photocatalytic performance of the AgCl-CN_x composites. In brief, the desired dosage of the AgCl-CN_x

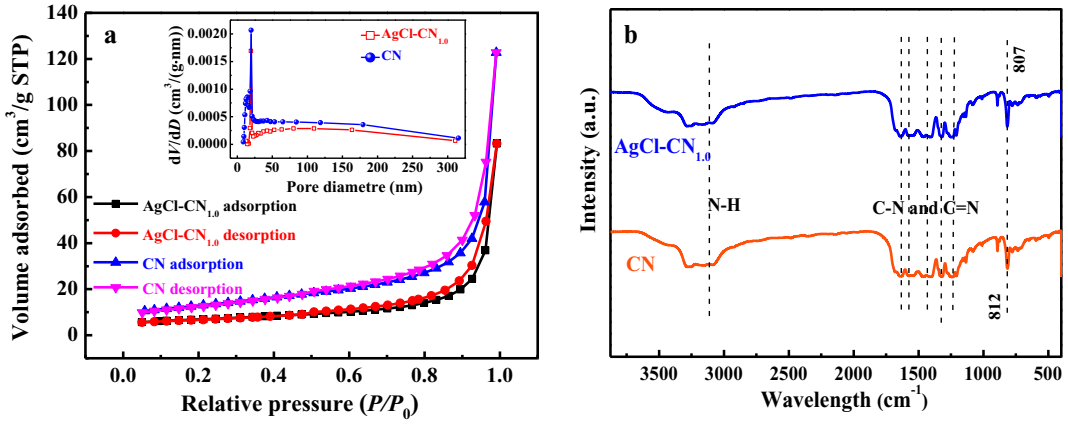

Fig. 3 – (a) Nitrogen adsorption/desorption isotherm and (inset) Barrett–Joyner–Halenda pore-size distribution plot and (b) Fourier transform infrared spectra of CN and AgCl-$CN_{1.0}$ composite. STP: standard temperature and pressure; d*V*/d*D*: aperture per unit aperture.

composites and OA stock solution were introduced into the 100 mL reactor. Diluted NaOH or HCl solution was employed to adjust the initial pH to the desired value. Prior to the irradiation, the suspension was pre-stirred vigorously for 30 min to establish adsorption–desorption equilibrium, then a 300 W Xenon lamp (PLS-SXE300, Perfectlight, China) coupled with an optical filter ($\lambda > 420$ nm) to cut off the light in the ultraviolet region, was used as the visible light source to irradiate the suspension. The reaction solution was kept at approximately 25°C with a circulating water bath and stirred with a magnetic stirrer throughout the experiment. Aliquots of the suspension were collected at different irradiation time intervals, filtered to remove the photocatalysts, and stored at 4°C for further analysis.

1.5. *Analytical methods*

The OA concentration was analyzed by a high-performance liquid chromatography (HPLC, e2695, Waters, USA) system equipped with a C18 column (150 mm × 4.6 mm, 5 μm

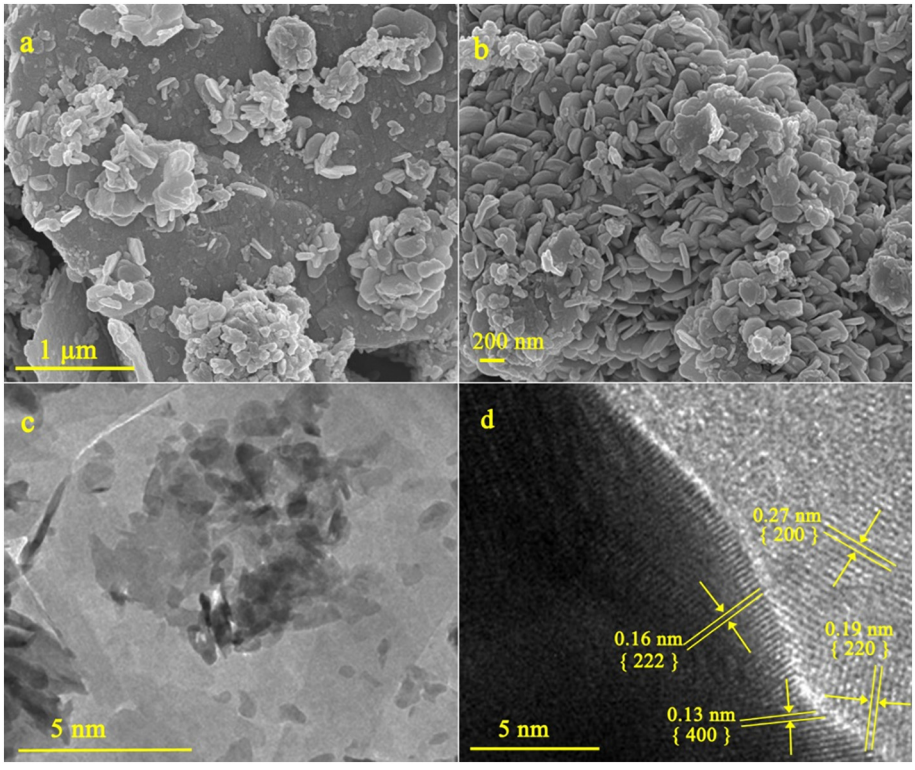

Fig. 4 – (a,b) Scanning electron microscopy and (c,d) transmission electron microscopy images of AgCl-$CN_{1.0}$ composite.

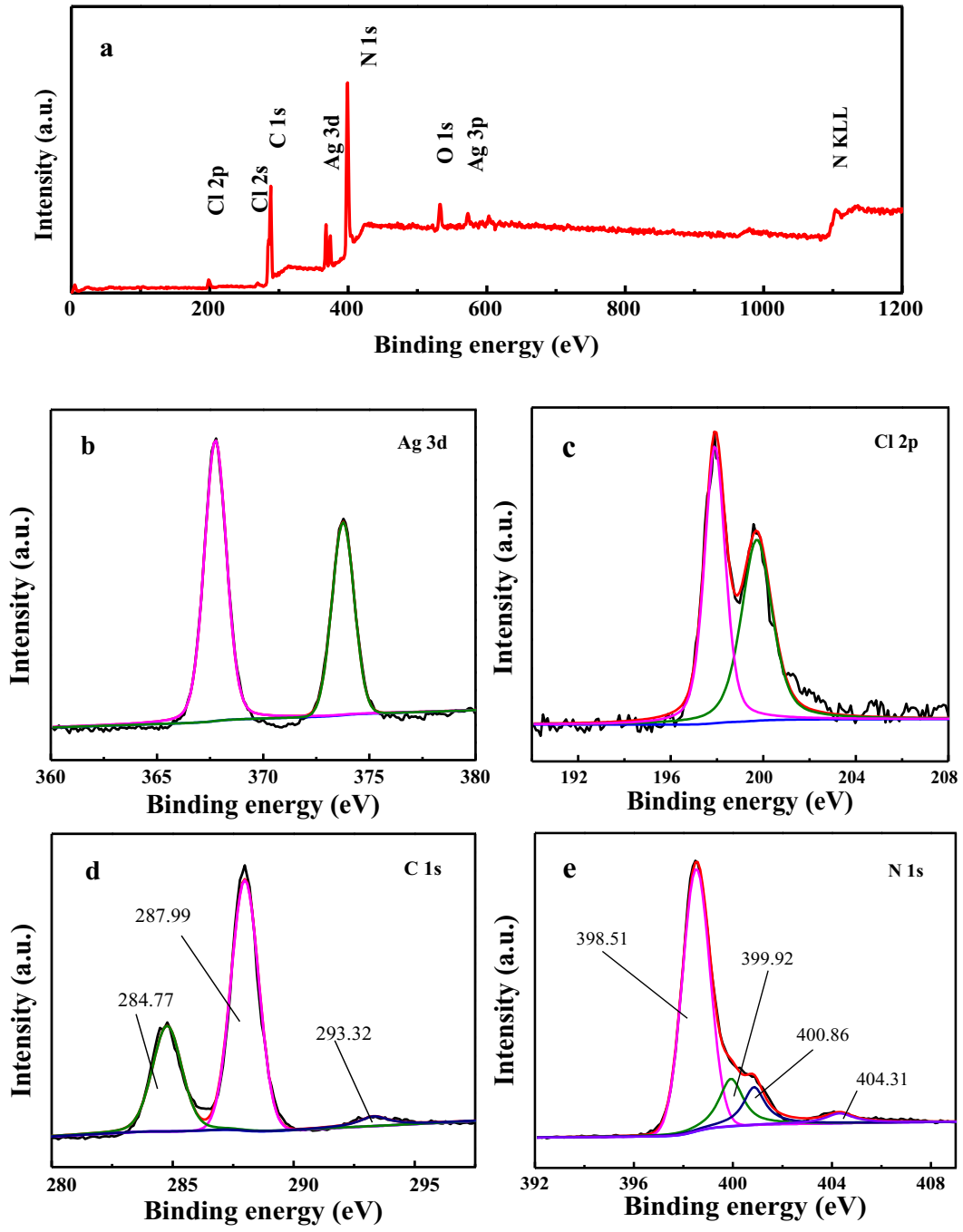

Fig. 5 – X-ray photoelectron spectroscopy spectra of (a) survey, (b) Ag 3d, (c) Cl 2p, (d) N 1s and (e) C 1s for AgCl-$CN_{1.0}$ composite. N KLL: Auger peak of nitrogen.

particle size) and UV–Vis detector (2489, Waters, USA). The total organic carbon (TOC) was monitored by TOC analyzer (vario, Elementar, Germany). The Ag^+ concentration in solution was quantified by an inductively coupled plasma-atomic emission spectrometer (ICP-AES, Optima 5300 DV, Perkin Elmer, USA). Free radicals during the reaction were trapped by DMPO (100 mmol/L) and determined by an electron spin resonance spectrometer (ESR, A300, Bruker, Germany).

2. Results and discussion

2.1. *Photocatalytic activity evaluation of AgCl-CN_x composites*

The photocatalytic performance of AgCl-CN_x composites was evaluated by the degradation of OA and the results are shown in Fig. 1a. The OA degradation generally followed pseudo-first-order kinetics. The OA removal in direct

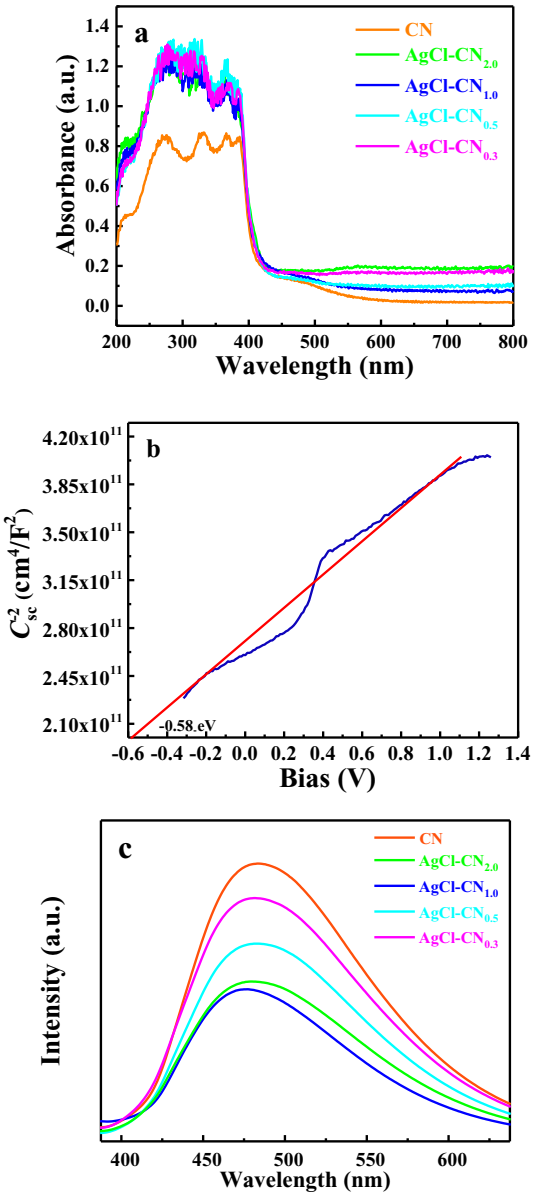

Fig. 6 – (a) Ultraviolet–visible diffuse reflectance spectra of CN and AgCl-CN$_x$ composites, (b) the Mott-Schottky curve of AgCl-CN$_{1.0}$, and (c) photoluminescence spectra of CN and AgCl-CN$_x$ composites. C_{sc}^{-2}: observed capacitance of semiconductor.

photolysis and the photocatalytic process with CN (the Vis/CN process) was negligible within 60 min (<5%). The photocatalytic activity of CN was significantly enhanced with the AgCl decoration. As depicted in Fig. 1b, an obvious enhancement of OA degradation was observed with the pseudo-first-order rate constant (k_{obs}) increasing from 0.0367 min^{-1} (R^2 = 0.9936) to 0.0722 min^{-1} (R^2 = 0.9728) with the decoration ratio ranging from 0.3 to 1.0. However, when the decoration ratio of AgCl further increased to 2.0, there was an obvious decrease on OA degradation, with k_{obs} declining to 0.0556 min^{-1} (R^2 = 0.9932). Therefore, the best photocatalytic activity was achieved with AgCl-CN$_{1.0}$ and the corresponding OA degradation efficiency was 98.02% within 60 min, which was about 80 times as high as that of the Vis/CN process.

2.2. Characterization of AgCl-CN$_x$ composites

A series of characterization techniques including XRD, BET, FT-IR, SEM, TEM, XPS, UV–Vis DRS, Mott–Schottky (M–S) analysis, and PL were carried out to determine the physico-chemical, microstructure, and optical properties of AgCl-CN$_x$ composites (especially AgCl-CN$_{1.0}$).

XRD was employed to investigate the crystal structure and chemical composition of AgCl-CN$_x$ composites, and their diffraction patterns are shown in Fig. 2a. For CN, a diffraction peak at 27.4° was clearly observed and indexed as (002), corresponding to the interlayer stacking of the conjugated aromatic structure (Mamba and Mishra, 2016; Patnaik et al., 2018). For AgCl-CN$_x$ composites, diffraction peaks centered at 27.8, 32.2, 46.2, 54.8, 57.4, 67.4, 74.4, and 76.7° could be indexed to the characteristic peaks of the (111), (200), (220), (311), (222), (400), (331), and (420) planes of AgCl (JCPDF 85-1355), respectively (Asadzadeh-Khaneghah et al., 2018; Liao et al., 2013). As presented in Fig. 2b, the diffraction peak intensity of AgCl was notably increased with the increment of the AgCl decoration ratio. Meanwhile, the diffraction peak of CN, which could be obscured by the peak of AgCl at 27.8°, was not distinctly observed in the AgCl-CN$_x$ composites. No clear diffraction peaks of metallic Ag or other impurities were detected in AgCl-CN$_x$ composites, indicating that CN and AgCl with high purity were obtained and coexisted.

The specific surface areas, pore volumes and pore diameter of CN and AgCl-CN$_x$ composites are shown in Table 1. With increasing AgCl decoration ratios from 0 to 2.0, the specific surface area of AgCl-CN$_x$ composites decreased from 44.7475 to 6.1542 m^2/g (Table 1). Meanwhile, as illustrated in Fig. 3a, the CN and AgCl-CN$_{1.0}$ samples exhibited nitrogen adsorption–desorption isotherms of type-IV with an H3 hysteresis loop, indicating the presence of mesoporous structures with main pore size of 10–30 nm (Yuan et al., 2018a). The mesopores probably originated from the stacking of irregular nanosheets and the thermal polymerization of CN. Besides, it can be noted from Table 1 and inset in Fig. 3a that with the augmentation of AgCl decoration ratio, the pore volume and mesoporosity of AgCl-CN$_x$ composites were apparently decreased. It is reasonable to deduce that the AgCl could be anchored on the surface of CN and that some mesopores may be obstructed by the particles. As exhibited in Fig. 1, the optimum photocatalytic activity was achieved with the AgCl-CN$_{1.0}$ composite, revealing that its moderate specific surface area and pore distribution could promote the adsorption, desorption, and diffusion of reactants and products, further enabling efficient OA degradation in the photocatalytic process (Wu et al., 2019).

Fig. 3b displays the FT-IR spectra of CN and the AgCl-CN$_{1.0}$ composite. In the case of CN, the bands in the range of 1250–1650 cm^{-1} were associated with the stretching vibrations of C–N and C=N in heterocycles, while the peak at 812 cm^{-1} was attributed to the characteristic breathing modes of s-triazine units. Additionally, the broad bands in the range of 3000–3500 cm^{-1} were ascribed to surface-adsorbed hydroxyl

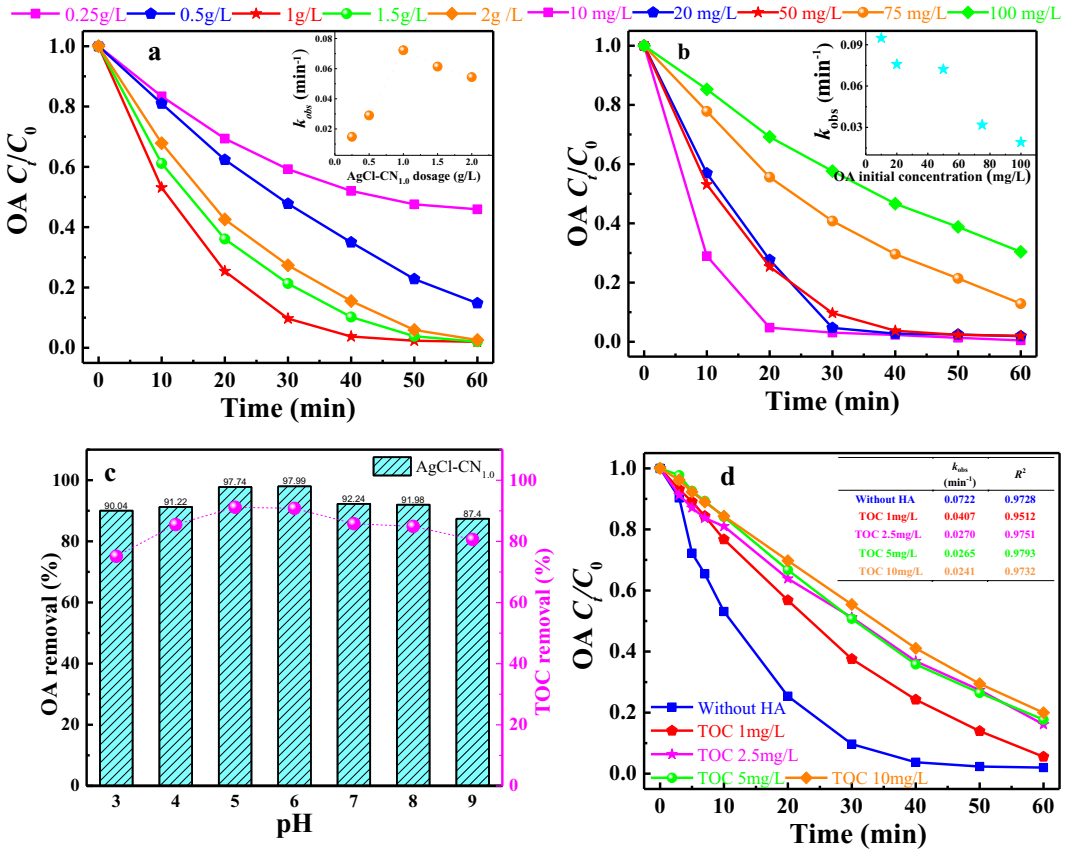

Fig. 7 – Effects of (a) AgCl-$CN_{1.0}$ dosage, (b) initial OA concentration, (c) solution pH, and (d) natural organic matter on OA degradation in AgCl-$CN_{1.0}$ process. Experimental conditions: [AgCl-$CN_{1.0}$] = 100 mg/L (except for (a)), $[OA]_0$ = 50 mg/L (except for (b)), pH_0 = 6.0 ± 0.1 (except for (c)), and *T* = 20°C. TOC: total organic carbon; HA: humic acid.

and N–H groups (Mamba and Mishra, 2016; Ong et al., 2016; Patnaik et al., 2018). For the AgCl-$CN_{1.0}$ composite, all the characteristic vibrational peaks of CN were observed, suggesting that the main structure of CN did not change, which was consistent with the XRD results. It can be seen from Fig. 3b that the band at 807 cm^{-1} of CN was slightly shifted to 812 cm^{-1} for the AgCl-$CN_{1.0}$ composite, implying strong interaction between CN and AgCl (Kang et al., 2015; Ong et al., 2016).

The morphology of the AgCl-$CN_{1.0}$ composite was further characterized by SEM and TEM. As shown in Fig. 4a, abundant AgCl particles were uniformly distributed on the laminated CN structure. The surface AgCl particles were observed to have an oblate flaky erythrocyte-like structure with size of 150–200 nm (Fig. 4b). It can be observed from Fig. 4c that the CN could act as a stable support in facilitating the uniform dispersion and the stability of AgCl particles. Moreover, the interplanar spacings of 0.13, 0.16, 0.19, and 0.27 nm were indexed to the (400), (222), (220), and (200) planes of AgCl, respectively (Asadzadeh-Khaneghah et al., 2018) (Fig. 4d), which was in accordance with the XRD results. In addition, TEM images also confirmed that the AgCl nanoparticles on the surface of CN could form a heterojunction structure, further improving the photocatalytic activity by suppressing the recombination rate of photogenerated charge carriers (Liang et al., 2019; Ong et al., 2016; Ou et al., 2018).

The chemical composition and electronic state of the AgCl-$CN_{1.0}$ composite were examined by XPS. Fig. 5a shows that the main elements in AgCl-$CN_{1.0}$ composite were Ag, Cl, C, N, and O, respectively. No characteristic peaks for elements other than Ag, Cl, C, N, and O can be observed in Fig. 5a, signifying

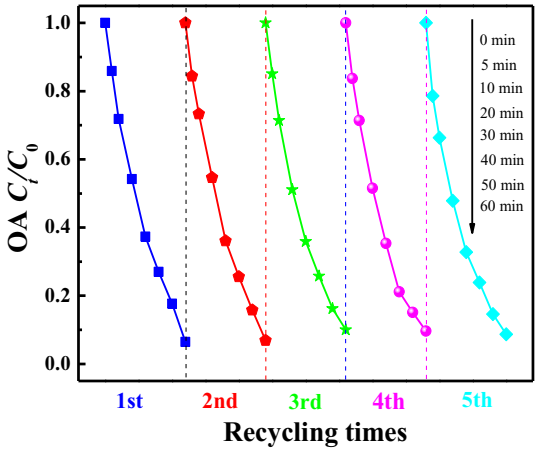

Fig. 8 – Recycling experiments of AgCl-$CN_{1.0}$. Experimental conditions: [AgCl-$CN_{1.0}$] = 100 mg/L, $[OA]_0$ = 50 mg/L, pH_0 = 6.0 ± 0.1, and *T* = 20°C.

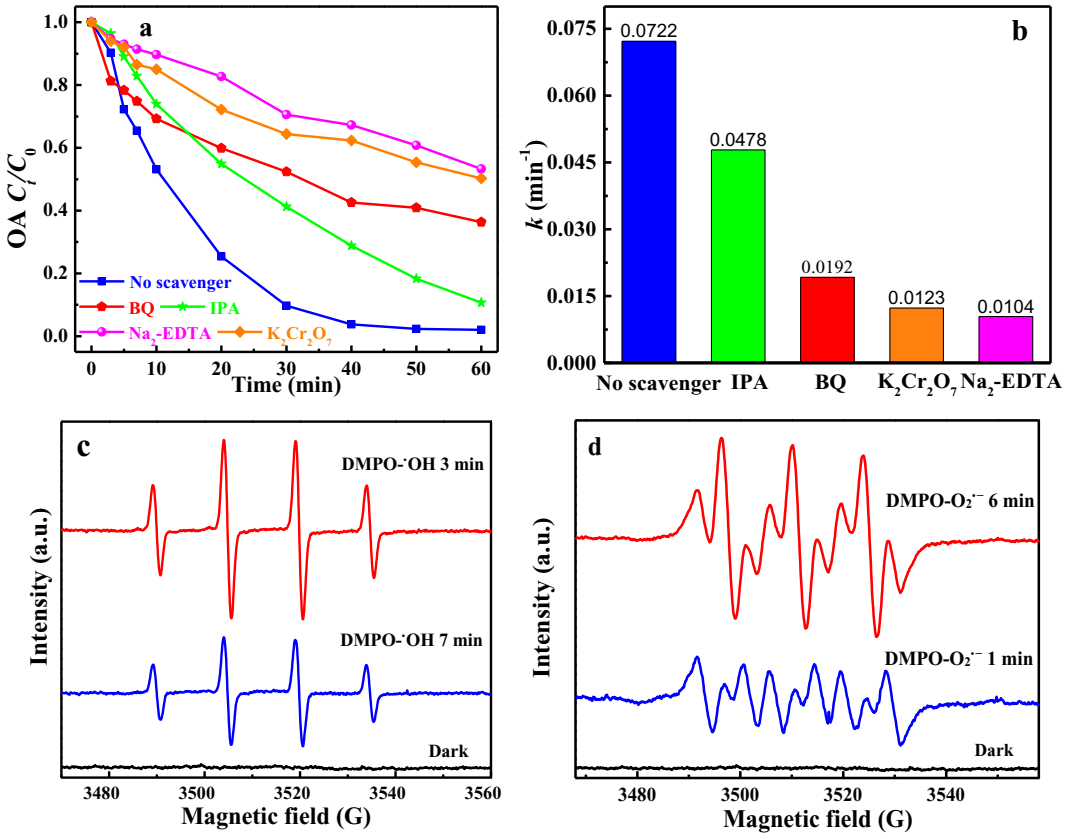

Fig. 9 – Effects of various scavengers on (a) OA degradation and (b) k_{obs} of OA degradation in AgCl-$CN_{1.0}$ composite and electron spin resonance spectra of (c) DMPO-·OH adducts in water and (d) DMPO-$O_2^{\cdot-}$ adducts in methanol under visible light irradiation. Experimental conditions: $[OA]_0$ = 50 mg/L, [AgCl-$CN_{1.0}$] = 100 mg/L, pH_0 = 6.0 ± 0.1, [BQ] = [IPA] = [Na_2-EDTA] = [$K_2Cr_2O_7$] = 100 mg/L, and T = 20°C. DMPO: 5,5-dimethyl-1-pyrolin-N-oxide; ·OH: hydroxyl radical; $O_2^{\cdot-}$: superoxide anion radical; BQ: *p*-benzoquinone; IPA: isopropanol; Na_2-EDTA: disodium ethylenediaminetetraacetate; $K_2Cr_2O_7$: potassium dichromate; *k*: rate constant.

the high purity of the AgCl-$CN_{1.0}$ composite. Meanwhile, the high resolution XPS spectra of Ag 3d, Cl 2p, C 1s, and N 1s are given in Fig. 5b–e. As presented in Fig. 5b, the Ag 3d spectrum exhibited two peaks at around 367.4 and 373.4 eV, which were ascribed to Ag $3d_{5/2}$ and $3d_{3/2}$, suggesting the typical binding energy of Ag^+ (Akhundi and Habibi-Yangjeh, 2015). In the Cl 2p spectrum (Fig. 5c), the main peaks centered at 197.5 and 199.0 eV can be assigned to the characteristic doublets of Cl $2p_{3/2}$ and $2p_{1/2}$ (Akhundi and Habibi-Yangjeh, 2015). The C 1 s spectrum in Fig. 5d was fitted with three peaks at 284.8, 288.0, and 293.3 eV, respectively. The major peak at 288.0 eV was derived from C=N–C in the CN network (Zhou et al., 2014). Then, the other two peaks at 284.8 and 293.3 eV corresponded to C=C and C=O groups, respectively (Zhou et al., 2014). For the N 1s spectrum shown in Fig. 5e, four different peaks at 398.5, 399.9, 400.9, and 404.2 eV were attributed to C=N–C, N–$(C)_3$ or H–N–$(C)_2$, C–N–H, and the special charging behavior of heterocycles, respectively (Li et al., 2017; Zhu et al., 2018).

The UV–Vis absorbance spectra of CN and AgCl-CN_x composites are shown in Fig. 6a. The light absorption edge of CN was 410 nm and its E_g was calculated to be 3.02 eV based on the Kubelka–Munk band-gap estimation theory (Zhu et al., 2018). With the AgCl decoration ratio increasing, the absorption edge of AgCl-CN_x composites did not vary notably, and the E_g of AgCl-$CN_{1.0}$ was estimated to be 3.00 eV. However, the absorption intensities of AgCl-CN_x composites in the

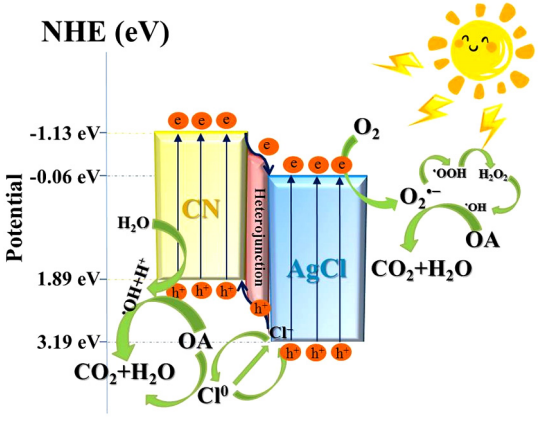

Fig. 10 – Possible mechanism of OA degradation in the photocatalytic process. NHE: normal hydrogen electron; e: electron; h^+: hole.

visible light region were slightly enhanced with the increment of AgCl decoration, which was in accordance with the photocatalytic activities of AgCl-CN_x composites. Furthermore, the positive slope of the M–S curve for the AgCl-$CN_{1.0}$ composite (Fig. 6b) indicated typical n-type semiconductor behavior, and that e were the majority charge carriers (Li et al., 2017; Zhu et al., 2018). The conduction band potential (E_{CB}) of CN and AgCl-$CN_{1.0}$ composite were calculated to be −1.13 and −0.58 eV, and their corresponding valence band potential (E_{VB}) were 1.89 and 2.42 eV, respectively. In addition, the E_{CB} and E_{VB} of AgCl have been reported to be −0.06 and 3.19 eV (Asadzadeh-Khaneghah et al., 2018; Li et al., 2017; Yang et al., 2017). Therefore, the difference in the positions of CN and AgCl energy bands created the prerequisite for the formation of a Type II heterojunction between AgCl and CN. In addition, the E_{CB} and E_{VB} of AgCl-$CN_{1.0}$ composite were higher compared with these of CN, resulting in stronger oxidizing ability and more favorable pollution degradation capability (Zhu et al., 2018).

Fig. 6c displays the PL spectra of CN and AgCl-CN_x composites at the excitation wavelength of 470 nm. It could be clearly observed that there was a significant decrease in the PL intensity of AgCl-CN_x composites compared to that of CN. The intensity of the PL peak is strongly related to the recombination of the e–h^+ pairs within the semiconductor (Xu et al., 2018b). Amongst the samples, the AgCl-$CN_{1.0}$ composite showed the weakest emission peak centered at around 470 nm (Fig. 6c), which was in good agreement with the results of its photocatalytic activity. Therefore, it can be concluded that in the case of the AgCl-$CN_{1.0}$ composite, the photogenerated e–h^+ pairs can efficiently transfer at the interface of the heterostructure, resulting in the highest photocatalytic activity under visible light.

2.3. Photocatalytic performance for AgCl-$CN_{1.0}$ composite

The photocatalytic performance of the AgCl-$CN_{1.0}$ composite was evaluated by the degradation of OA under visible light. The effects of several operational parameters (i.e., AgCl-$CN_{1.0}$ dosage, initial OA concentration, solution pH, and NOM) on OA degradation efficiency were systematically investigated.

The effects of AgCl-$CN_{1.0}$ dosage from 0.25 to 2 g/L on the OA degradation were investigated and the results are illustrated in Fig. 7a. A marked improvement of OA degradation was observed with the increase of AgCl-$CN_{1.0}$ dosage in the range of 0.25–1 g/L, with k_{obs} increasing from 0.0148 min^{-1} (R^2 = 0.9458) to 0.0722 min^{-1} (R^2 = 0.9728). However, when the AgCl-$CN_{1.0}$ dosage was further raised to 2 g/L, there was a distinct decrease in OA removal, with k_{obs} declining to 0.0544 min^{-1} (R^2 = 0.9568). Therefore, the presence of the AgCl-$CN_{1.0}$ composite at low dosage under visible light could apparently enhance the production of h^+ and e, promoting the elimination of OA, while at high dosage (2 g/L), the self-aggregation of AgCl-$CN_{1.0}$ would partially inhibit the penetration of visible light into the solution (Akbarzadeh et al., 2018; Cai et al., 2016).

The OA degradation at initial concentrations varying from 10 to 100 mg/L is displayed in Fig. 7b. The k_{obs} of OA degradation drastically decreased from 0.0948 min^{-1} (R^2 = 0.9013) to 0.0192 min^{-1} (R^2 = 0.9967) when the initial OA concentration increased from 10 to 100 mg/L. This phenomenon can be attributed to the fact that the catalyst active sites may be saturated by pollutant molecules at a high initial concentration. Besides, a higher initial concentration yielded a higher concentration of intermediates to compete with OA for the available oxidants (Yuan et al., 2018b). Therefore, the initial OA concentration of 50 mg/L was selected in this study to simulate practical conditions and to ensure a sufficient amount of OA degradation.

As illustrated in Fig. 7c, the effects of solution pH on OA degradation and mineralization in the photocatalytic process of AgCl-$CN_{1.0}$ (the Vis/AgCl-$CN_{1.0}$ process) were investigated from pH 3–9. At all studied pH values, AgCl-$CN_{1.0}$ achieved an excellent OA removal rate and over 87.41% of OA was eliminated within 60 min. Notably, OA was scarcely removed (less than 2%) by direct photodegradation and AgCl-$CN_{1.0}$ adsorption under all the experimental pH conditions (data not shown in Fig. 7c). In addition, the OA mineralization rates at pH values of 3, 4, 5, 6, 7, 8, and 9 within 60 min were 81.72%, 86.37%, 91.18%, 90.81%, 85.82%, 84.88%, and 80.64%, respectively, which corresponded well with the OA degradation efficiency at each pH value. The results suggested that AgCl-$CN_{1.0}$ exhibited superior photocatalytic performance under both acidic and alkaline conditions, demonstrating its great potential for use in practical wastewater treatment.

NOM is ubiquitous in surface water, ground water, and wastewater. HA, as an important component of NOM, can directly or indirectly react with reactive species to affect the degradation of organic compounds during photocatalysis. The effects of HA on OA degradation in the Vis/AgCl-$CN_{1.0}$ process are displayed in Fig. 7d. With the increase in concentration of HA from 0 to 10 mg/L (as TOC), the k_{obs} of OA degradation declined from 0.0428 min^{-1} (R^2 = 0.9804) to 0.0241 min^{-1} (R^2 = 0.9732). As the HA concentration rose, HA could affect the penetration of visible light and also compete with OA for active substances, thus inhibiting the OA degradation (Brezonik, 1994; Yuan et al., 2019). Nevertheless, even in the presence of HA, AgCl-$CN_{1.0}$ exhibited great photocatalytic performance, and over 80% of OA could be degraded in the Vis/AgCl-$CN_{1.0}$ process within 60 min.

2.4. Stability of the AgCl-$CN_{1.0}$ composite

The stability of the photocatalyst is a crucial factor in practical application. As shown in Fig. 8, there was no observable loss of photocatalytic performance of AgCl-$CN_{1.0}$ composite after five runs and the OA removal efficiency still reached 92.03%. In addition, the characteristic peaks of reused AgCl-$CN_{1.0}$ showed little shift and the diffraction intensity at 27.8° was only slightly decreased compared with that of fresh AgCl-$CN_{1.0}$, indicating that the structure of AgCl-$CN_{1.0}$ was relatively stable. Moreover, it is noted that the release of Ag^+ into the solution was relatively low (<0.01 mg/L) in the Vis/AgCl-$CN_{1.0}$ process (under different pH values). Overall, AgCl-$CN_{1.0}$ represented great reusability and stability in the photocatalytic process, which provides strong justification for its practical application in environmental remediation.

2.5. Possible photocatalytic mechanism of AgCl-$CN_{1.0}$

To clarify the degradation mechanisms in the Vis/AgCl-$CN_{1.0}$ process, the possible reactive species for the OA degradation were investigated by radical scavenger experiments. IPA, Na_2-EDTA, BQ, and $K_2Cr_2O_7$ were used as scavengers for hydroxyl radical ($^{\bullet}OH$), h^+, superoxide anion radical ($O_2^{\bullet-}$), and e, respectively (Cai et al., 2016; Yao et al., 2015; Zhou et al., 2014). As depicted in Fig. 9a, the photocatalytic performance was greatly inhibited by the addition of the scavengers (following the order Na_2-EDTA > $K_2Cr_2O_7$ > BQ > IPA). With no addition of scavengers, about 98.02% of OA was degraded in 60 min, while the presence of IPA, Na_2-EDTA, BQ and $K_2Cr_2O_7$ resulted in decreasing the OA removal to 89.34%, 46.75%, 63.34%, and 49.73% within 60 min, respectively. The results revealed that h^+, e, $O_2^{\bullet-}$, and $^{\bullet}OH$ were the dominant reactive radicals participating in the Vis/AgCl-$CN_{1.0}$ process. Moreover, the involvement of $^{\bullet}OH$ and $O_2^{\bullet-}$ in the Vis/AgCl-$CN_{1.0}$ process can be further identified by the ESR technique with DMPO as a spin trap agent (Wang et al., 2011). As illustrated in Fig. 9b–c, a typical four-line signal with a peak intensity ratio of 1:2:2:1 corresponded to the DMPO-$^{\bullet}OH$ adduct, confirming the formation of $^{\bullet}OH$ (Zhang et al., 2017). Additionally, the sextet ESR signal assigned to the DMPO-$O_2^{\bullet-}$ adduct was also detected, indicating the presence of $O_2^{\bullet-}$ in the Vis/AgCl-$CN_{1.0}$ process (Hong et al., 2018).

Based on the aforementioned results, a possible photocatalytic mechanism for AgCl-$CN_{1.0}$ is proposed in Fig. 10. Under visible light irradiation, both CN and AgCl can be excited, and yield e and h^+ in their conduction band (CB) and valence band (VB) (Eqs. (1)–(2)), creating e–h^+ pairs. Furthermore, the Type II heterojunction between AgCl and CN became a crucial bridge, allowing for the transfer of h^+ from the VB of AgCl to the VB of CN while shift from the CB of CN to the CB of AgCl (Murugesan et al., 2018; Ong et al., 2016; An et al., 2016; Hu et al., 2018). In addition, the h^+ can oxidize Cl^- to Cl^0. Cl^0 could carry out oxidation of OA to generate Cl^-, further combining with Ag^+ to reform AgCl again (Eqs. (3)–(5)) (Meng et al., 2016; Yao et al., 2015). Moreover, photoexcited e in the CB of AgCl (E_{CB} = −0.06 eV) could reduce O_2 to generate $O_2^{\bullet-}$ because the E_{CB} of AgCl-$CN_{1.0}$ was more negative than the reduction potential of $E(O_2/O_2^{\bullet-})$ = −0.33 eV per normal hydrogen electron, which was conducive to the degradation of OA (Eqs. (6)–(7)) (Yao et al., 2015). In addition, the generation of $^{\bullet}OH$ can probably attributed to transformation from $O_2^{\bullet-}$ and h^+, as displayed in Eqs. (8)–(11) (Huo et al., 2018; Liu et al., 2018a, 2018c), which further participated in the mineralization of OA (Eq. (12)).

$$CN \xrightarrow{h\nu} CN(e_{CB}) + CN(h^+_{VB}) \quad (1)$$

$$AgCl \xrightarrow{h\nu} AgCl(e_{CB}) + AgCl(h^+_{VB}) \quad (2)$$

$$AgCl + h^+ \rightarrow Ag^+ + Cl^0 \quad (3)$$

$$Cl^0 + OA \rightarrow Cl^- + CO_2 + H_2O \quad (4)$$

$$Ag^+ + Cl^- \rightarrow AgCl \quad (5)$$

$$O_2 + e \rightarrow O_2^{\bullet-} \quad (6)$$

$$O_2^{\bullet-} + OA \rightarrow CO_2 + H_2O \quad (7)$$

$$h^+ + H_2O \rightarrow {}^{\bullet}OH + H^+ \quad (8)$$

$$O_2^{\bullet-} + H^+ \rightarrow {}^{\bullet}OOH \quad (9)$$

$${}^{\bullet}OOH + H^+ + e \rightarrow H_2O_2 \quad (10)$$

$$H_2O_2 + e \rightarrow {}^{\bullet}OH + OH^- \quad (11)$$

$${}^{\bullet}OH + OA \rightarrow H_2O + CO_2 \quad (12)$$

3. Conclusions

In summary, AgCl-CN_x composites prepared by a simple precipitation-reflux method were found to be highly efficient for OA degradation under visible light. Further, AgCl-$CN_{1.0}$ exhibited excellent photocatalytic performance under both acidic and alkaline conditions, and achieved the optimum photocatalytic activity at pH = 6, achieving 98.02% OA degradation efficiency within 60 min. AgCl-$CN_{1.0}$ was observed to have an oblate flaky erythrocyte-like structure and formed a Type II heterojunction structure. The E_{CB} and E_{VB} of AgCl-$CN_{1.0}$ were calculated to be −0.58 and 2.42 eV, resulting in strong oxidizing ability. The suitable E_g (~3.00 eV) and the presence of a heterojunction could effectively reduce the e–h^+ pair recombination rate of AgCl-$CN_{1.0}$, promoting the photocatalytic activity. The species h^+, e, $O_2^{\bullet-}$, and $^{\bullet}OH$ were identified as the dominant reactive species in the Vis/AgCl-$CN_{1.0}$ process. Furthermore, AgCl-$CN_{1.0}$ exhibited considerable stability and effective activity towards the mineralization of OA, making it a promising candidate for use in environmental remediation.

Acknowledgments

This work was supported by the National Natural Science Foundation of China (No. 51808412), the Natural Science Foundation of Hubei province (Nos. 2017CFA026 and 2018CFB266), the Central Government Guidance for Local Science and Technology Development Projects for Hubei province (No. 2018ZYYD024) and the Science and Technology Project of Educational Commission of Hubei province (No. Q20181706).

REFERENCES

Akbarzadeh, R., Fung, C.S.L., Rather, R.A., Lo, I.M.C., 2018. One-pot hydrothermal synthesis of g-C_3N_4/Ag/AgCl/$BiVO_4$ micro-flower composite for the visible light degradation of ibuprofen. Chem. Eng. J. 341, 248–261.

Akhundi, A., Habibi-Yangjeh, A., 2015. Ternary g-C_3N_4/ZnO/AgCl nanocomposites: synergistic collaboration on visible-light-driven activity in photodegradation of an organic pollutant. Appl. Surf. Sci. 358, 261–269.

An, J.J., Zhang, G.Y., Zheng, R.F., Wang, P., 2016. Removing lignin model pollutants with $BiFeO_3$–g-C_3N_4 compound as an

efficient visible-light-heterogeneous Fenton-like catalyst. J. Environ. Sci. 48, 218–229.
Asadzadeh-Khaneghah, S., Habibi-Yangjeh, A., Abedi, M., 2018. Decoration of carbon dots and AgCl over g-C_3N_4 nanosheets: novel photocatalysts with substantially improved activity under visible light. Sep. Purif. Technol. 199, 64–77.
Asahi, R., Morikawa, T., Ohwaki, T., Aoki, K., Taga, Y., 2001. Visible-light photocatalysis in nitrogen-doped titanium oxides. Science 293, 269.
Bellardita, M., García-López, E.I., Marcì, G., Krivtsov, I., García, J.R., Palmisano, L., 2018. Selective photocatalytic oxidation of aromatic alcohols in water by using P-doped g-C_3N_4. Appl. Catal. B Environ. 220, 222–233.
Brezonik, P.L., 1994. Chemical Kinetics and Process Dynamics in Aquatic Systems. Lewis, Boca Raton.
Cai, C., Zhang, Z.Y., Liu, J., Shan, N., Zhang, H., Dionysiou, D.D., 2016. Visible light-assisted heterogeneous Fenton with $ZnFe_2O_4$ for the degradation of Orange II in water. Appl. Catal. B Environ. 182, 456–468.
Dong, H., Guo, X.T., Yang, C., Ouyang, Z.Z., 2018. Synthesis of g-C_3N_4 by different precursors under burning explosion effect and its photocatalytic degradation for tylosin. Appl. Catal. B Environ. 230, 65–76.
Hong, Y.Z., Li, C.S., Yin, B.X., Li, D., Zhang, Z.Y., Mao, B.D., et al., 2018. Promoting visible-light-induced photocatalytic degradation of tetracycline by an efficient and stable beta-Bi_2O_3@g-C_3N_4 core/shell nanocomposite. Chem. Eng. J. 338, 137–146.
Hu, M.Q., Xing, Z.P., Cao, Y., Li, Z.Z., Yan, X., Xiu, Z.Y., et al., 2018. Ti^{3+} self-doped mesoporous black TiO_2/SiO_2/g-C_3N4 sheets heterojunctions as remarkable visible-lightdriven photocatalysts. Appl. Catal. B Environ. 226, 499–508.
Huo, R., Yang, X.L., Yang, J.Y., Yang, S.Y., Xu, Y.H., 2018. Self-assembly synthesis of $BiVO_4$/Polydopamine/g-C_3N_4 with enhanced visible light photocatalytic performance. Mater. Res. Bull. 98, 225–230.
Jiang, L.B., Yuan, X.Z., Pan, Y., Liang, J., Zeng, G.M., Wu, Z.B., et al., 2017. Doping of graphitic carbon nitride for photocatalysis: a review. Appl. Catal. B Environ. 217, 388–406.
Kang, S.F., Fang, Y., Huang, Y.K., Cui, L.-F., Wang, Y.Z., Qin, H.F., et al., 2015. Critical influence of g-C_3N_4 self-assembly coating on the photocatalytic activity and stability of Ag/AgCl microspheres under visible light. Appl. Catal. B Environ. 168-169, 472–482.
Kumar, A., Kumar, A., Sharma, G., Al-Muhtaseb, A.H., Naushad, M., Ghfar, A.A., et al., 2018. Quaternary magnetic BiOCl/g-C_3N_4/Cu_2O/Fe_3O_4 nano-junction for visible light and solar powered degradation of sulfamethoxazole from aqueous environment. Chem. Eng. J. 334, 462–478.
Li, J.Q., Hao, H.J., Zhou, J., Li, W.J., Lei, N., Guo, L., 2017. Ag@AgCl QDs decorated g-C_3N_4 nanoplates: the photoinduced charge transfer behavior under visible light and full arc irradiation. Appl. Surf. Sci. 422, 626–637.
Li, C.Q., Sun, Z.M., Zhang, W.Z., Yu, C.H., Zheng, S.L., 2018. Highly efficient g-C_3N_4/TiO_2/kaolinite composite with novel three-dimensional structure and enhanced visible light responding ability towards ciprofloxacin and S. aureus. Appl. Catal. B Environ. 220, 272–282.
Liang, S.H., Zhang, D.F., Pu, X.P., Yao, X.T., Han, R.T., Yin, J., et al., 2019. A novel Ag_2O/g-C_3N_4 p-n heterojunction photocatalysts with enhanced visible and near-infrared light activity. Sep. Purif. Technol. 210, 786–797.
Liao, W.J., Zhang, Y.R., Zhang, M., Murugananthan, M., Yoshihara, S., 2013. Photoelectrocatalytic degradation of microcystin-LR using Ag/AgCl/TiO_2 nanotube arrays electrode under visible light irradiation. Chem. Eng. J. 231, 455–463.
Liu, J.N., Jia, Q.H., Long, J.L., Wang, X.X., Gao, Z.W., Gu, Q., 2018a. Amorphous NiO as co-catalyst for enhanced visible-light-driven hydrogen generation over g-C_3N_4 photocatalyst. Appl. Catal. B Environ. 222, 35–43.
Liu, Y., Kong, J.J., Yuan, J.L., Zhao, W., Zhu, X., Sun, C., et al., 2018b. Enhanced photocatalytic activity over flower-like sphere Ag/Ag_2CO_3/$BiVO_4$ plasmonic heterojunction photocatalyst for tetracycline degradation. Chem. Eng. J. 331, 242–254.
Liu, X., Liang, J.T., Song, X.L., Yang, H.M., Li, X.J., Dai, H.Y., et al., 2018c. Enhanced water dissociation performance of graphitic-C_3N_4 assembled with ZnCr-layered double hydroxide. Chem. Eng. J. 337, 560–566.
Liu, Q.X., Zeng, C.M., Ai, L.H., Hao, Z., Jiang, J., 2018d. Boosting visible light photoreactivity of photoactive metal-organic framework: designed plasmonic Z-scheme Ag/AgCl@MIL-53-Fe. Appl. Catal. B Environ. 224, 38–45.
Mamba, G., Mishra, A.K., 2016. Graphitic carbon nitride (g-C_3N_4) nanocomposites: a new and exciting generation of visible light driven photocatalysts for environmental pollution remediation. Appl. Catal. B Environ. 198, 347–377.
Meng, A., Xing, J., Li, Z.J., Wei, Q., Li, Q.D., 2016. Ag/AgCl/ZnO nano-networks: preparation, characterization, mechanism and photocatalytic activity. J. Mol. Catal. A Chem. 411, 290–298.
Miao, X.L., Yue, X.Y., Ji, Z.Y., Shen, X.P., Zhou, H., Liu, M.M., et al., 2018. Nitrogen-doped carbon dots decorated on g-C_3N_4/Ag_3PO_4 photocatalyst with improved visible light photocatalytic activity and mechanism insight. Appl. Catal. B Environ. 227, 459–469.
Murugesan, P., Narayanan, S., Manickam, M., Murugesan, P.K., Subbiah, R., 2018. A direct Z-scheme plasmonic AgCl@g-C_3N_4 heterojunction photocatalyst with superior visible light CO_2 reduction in aqueous medium. Appl. Surf. Sci. 450, 516–526.
Oh, W.D., Lok, L.W., Veksha, A., Giannis, A., Lim, T.T., 2018. Enhanced photocatalytic degradation of bisphenol A with Ag-decorated S-doped g-C_3N_4 under solar irradiation: performance and mechanistic studies. Chem. Eng. J. 333, 739–749.
Ong, W.J., Putri, L.K., Tan, L.L., Chai, S.P., Yong, S.T., 2016. Heterostructured AgX/g-C_3N_4 (X=Cl and Br) nanocomposites via a sonication-assisted deposition-precipitation approach: emerging role of halide ions in the synergistic photocatalytic reduction of carbon dioxide. Appl. Catal. B Environ. 180, 530–543.
Ou, M., Wan, S.P., Zhong, Q., Zhang, S.L., Song, Y., Guo, L.N., et al., 2018. Hierarchical Z-scheme photocatalyst of g-C_3N_4@Ag/$BiVO_4$ (040) with enhanced visible-light-induced photocatalytic oxidation performance. Appl. Catal. B Environ. 221, 97–107.
Patnaik, S., Sahoo, D.P., Parida, K., 2018. An overview on Ag modified g-C_3N_4 based nanostructured materials for energy and environmental applications. Renew. Sust. Energ. Rev. 82, 1297–1312.
Qian, X.F., Wu, Y.W., Kan, M., Fang, M.Y., Yue, D.T., Zeng, J., et al., 2018. FeOOH quantum dots coupled g-C_3N_4 for visible light driving photo-Fenton degradation of organic pollutants. Appl. Catal. B Environ. 237, 513–520.
Wang, Z.H., Ma, W.H., Chen, C.C., Ji, H.W., Zhao, J.C., 2011. Probing paramagnetic species in titania-based heterogeneous photocatalysis by electron spin resonance (ESR) spectroscopy—a mini review. Chem. Eng. J. 170, 353–362.
Wang, Y., Tan, G.Q., Liu, T., Su, Y.N., Ren, H.J., Zhang, X.L., et al., 2018. Photocatalytic properties of the g-C_3N_4/{010} facets $BiVO_4$ interface Z-scheme photocatalysts induced by $BiVO_4$ surface heterojunction. Appl. Catal. B Environ. 234, 37–49.
Wu, X.F., Cheng, J.H., Li, X.F., Li, Y.H., Lv, K.L., 2019. Enhanced visible photocatalytic oxidation of NO by repeated calcination of g-C_3N_4. Appl. Surf. Sci. 465, 1037–1046.
Xu, S.Q., Zhu, H.X., Cao, W.R., Wen, Z.B., Wang, J.N., François-Xavier, C.P., et al., 2018a. Cu-Al_2O_3-g-C_3N_4 and Cu-Al_2O_3-C-dots with dual-reaction centres for simultaneous enhancement of Fenton-like catalytic activity and selective H_2O_2 conversion to hydroxyl radicals. Appl. Catal. B Environ. 234, 223–233.
Xu, Y.X., Lin, D.F., Liu, X.P., Luo, Y.J., Xue, H., Huang, B.Q., et al., 2018b. TiO_2 hollow nanofibers grafted Ag/AgCl with more AgCl

{111} facet for enhanced photocatalytic activity. Mater. Lett. 215, 250–253.

Yang, S.B., Xu, D.B., Chen, B.Y., Luo, B.F., Shi, W.D., 2017. In-situ synthesis of a plasmonic Ag/AgCl/Ag2O heterostructures for degradation of ciprofloxacin. Appl. Catal. B Environ 204, 602–610.

Yao, X.X., Liu, X.H., Zhu, D., Zhao, C.B., Lu, L.D., 2015. Synthesis of cube-like Ag/AgCl plasmonic photocatalyst with enhanced visible light photocatalytic activity. Catal. Commun. 59, 151–155.

Yuan, X.J., Duan, S.L., Wu, G.Y., Sun, L., Cao, G., Xia, D.S., et al., 2018a. Enhanced catalytic ozonation performance of highly stabilized mesoporous ZnO doped g-C_3N_4 composite for efficient water decontamination. Appl. Catal. A Gen. 551, 129–138.

Yuan, X.J., Qin, W.L., Lei, X.M., Sun, L., Li, Q., Xia, D.S., et al., 2018b. Efficient enhancement of ozonation performance via ZVZ immobilized g-C_3N_4 towards superior oxidation of micropollutants. Chemosphere 205, 369–379.

Yuan, X.J., Xie, R.L., Zhang, Q., Sun, L., Long, X.J., Xia, D.S., 2019. Oxygen functionalized graphitic carbon nitride as an efficient metal-free ozonation catalyst for atrazine removal: performance and mechanism. Sep. Purif. Technol. 211, 823–831.

Zhang, S., Quan, X., Zheng, J.F., Wang, D., 2017. Probing the interphase "HO· zone" originated by carbon nanotube during catalytic ozonation. Water Res. 122, 86–95.

Zheng, Y., Liu, J., Liang, J., Jaroniec, M., Qiao, S.Z., 2012. Graphitic carbon nitride materials: controllable synthesis and applications in fuel cells and photocatalysis. Energy Environ. Sci. 5, 6717–6731.

Zhou, T., Xu, Y.G., Xu, H., Wang, H.F., Da, Z.L., Huang, S.Q., et al., 2014. In situ oxidation synthesis of visible-light-driven plasmonic photocatalyst Ag/AgCl/g-C_3N_4 and its activity. Ceram. Int. 40, 9293–9301.

Zhu, Z.D., Pan, H.H., Murugananthan, M., Gong, J.Y., Zhang, Y.R., 2018. Visible light-driven photocatalytically active g-C_3N_4 material for enhanced generation of H_2O_2. Appl. Catal. B Environ. 232, 19–25.